

# $k$ -Space Deep Learning for Reference-free EPI Ghost Correction

Juyoung Lee, Yoseob Han, and Jong Chul Ye\*, *Senior Member, IEEE*

**Abstract**—Nyquist ghost artifacts in EPI images are originated from phase mismatch between the even and odd echoes. However, conventional correction methods using reference scans often produce erroneous results especially in high-field MRI due to the non-linear and time-varying local magnetic field changes. Recently, it was shown that the problem of ghost correction can be transformed into  $k$ -space data interpolation problem that can be solved using the annihilating filter-based low-rank Hankel structured matrix completion approach (ALOHA). Another recent discovery has shown that the deep convolutional neural network is closely related to the data-driven Hankel matrix decomposition. By synergistically combining these findings, here we propose a  $k$ -space deep learning approach that immediately corrects the  $k$ -space phase mismatch without a reference scan. Reconstruction results using 7T in vivo data showed that the proposed reference-free  $k$ -space deep learning approach for EPI ghost correction significantly improves the image quality compared to the existing methods, and the computing time is several orders of magnitude faster.

**Index Terms**—MRI, EPI, Nyquist ghost artifact, deep learning

## I. INTRODUCTION

Echo-planar imaging (EPI) is one of the widely used MR imaging sequences. This sequence is fast because the whole  $k$ -space data is acquired through a single RF pulse by alternating the magnetic field direction in the even and odd lines. This short scan provides high temporal resolution and has therefore been used in many imaging modalities such as functional MRI, diffusion-weighted imaging (DWI) and so on. However, the rapid change of the magnetic field direction for each line causes the induction of eddy currents in coils and the magnet housing. These eddy currents, in turn, generate local fields that distort  $B_0$  and produce a phase mismatch between even and odd rows. Due to this phase disparity, EPI images suffer from artifacts often called the  $N/2$ -Nyquist ghost artifact. Since this artifact overlaps with the original image, it often causes difficulties in analyzing the reconstruction result.

There have been many studies to remove ghost artifact. One of the most widely used methods to remove ghost artifact is a navigator-based method [1]–[4]. In this method, a pre-scanning, often called as reference or navigator scan, is separately acquired before an EPI scan to compensate for the phase mismatch. Most popular and simplest approach is to use  $k$ -space lines without phase encoding gradient so that the phase

difference between even and odd lines can be calculated. Then, the phase correction is performed across all phase encoding lines assuming that the phase offset varies linearly. However, this method suffers from many disadvantages. Aside from the additional acquisition time from the pre-scan at every imaging slice, the linearity assumption for the phase variation is not sufficiently accurate especially for high-field MR acquisition due to the complicated field inhomogeneity variations. Moreover, the current fMRI protocol acquires reference scan only once at the beginning, so it is difficult to capture time-varying local field fluctuations. To address ghost artifacts from these nonlinear and time-varying local field changes, navigator-free methods were proposed. Some researches with pulse sequence modification show the reduction of ghost artifact [5]–[11]. In addition, navigator-free methods without any pulse sequence modification have been also studied [7], [12], [13]. However, these classic navigator-free methods are generally ineffective compared to the reference-based methods.

Recently, high-performance reference-free EPI ghost correction have been proposed using low rank Hankel matrix completion approaches [14]–[16]. Pioneered by Lee et al [14] using the annihilating filter-based low-rank Hankel matrix approach (ALOHA) [17]–[19], the key idea is to take advantage of the fact that the concatenated Hankel matrix, which consists of even and odd  $k$ -space lines, has a low-rank structure due to redundancy. Thus, the phase mismatch correction problem can be converted to the missing  $k$ -space interpolation problem for even and odd  $k$ -space data that can be solved using low rank Hankel matrix completion. This method can be easily extended to parallel multi-coil imaging by simply stacking the Hankel matrices of each coil side-by-side and performing low-rank Hankel matrix completion. However, one of the main limitations of this approach is computational complexity due to matrix factorization. Thus, small size annihilating filter size is often used to reduce the computational complexity. However, this is not often robust in high field MRI such that it can not correct the ghost artifacts in some frames.

Therefore, the main goal of this work is to develop a robust and computational efficient ghost correction method that is suitable for high field MRI. In particular, inspired by the recent mathematical discovery showing that the deep convolutional neural network (CNN) is closely related to the Hankel matrix decomposition [20], we propose a novel  $k$ -space deep learning method for correcting ghost artifacts. More specifically, similar to the ALOHA-based ghost correction, we transform the ghost correction problem into the even and odd *virtual*  $k$ -space interpolation problem so that  $k$ -space deep neural networks can be designed to estimate the missing  $k$ -space lines. The

Authors are with the Department of Bio and Brain Engineering, Korea Advanced Institute of Science and Technology (KAIST), Daejeon 34141, Republic of Korea (e-mail: {juyounglee,hanyoseob,jong.ye}@kaist.ac.kr). This work is supported by National Research Foundation of Korea, Grant number NRF2016R1A2B3008104.

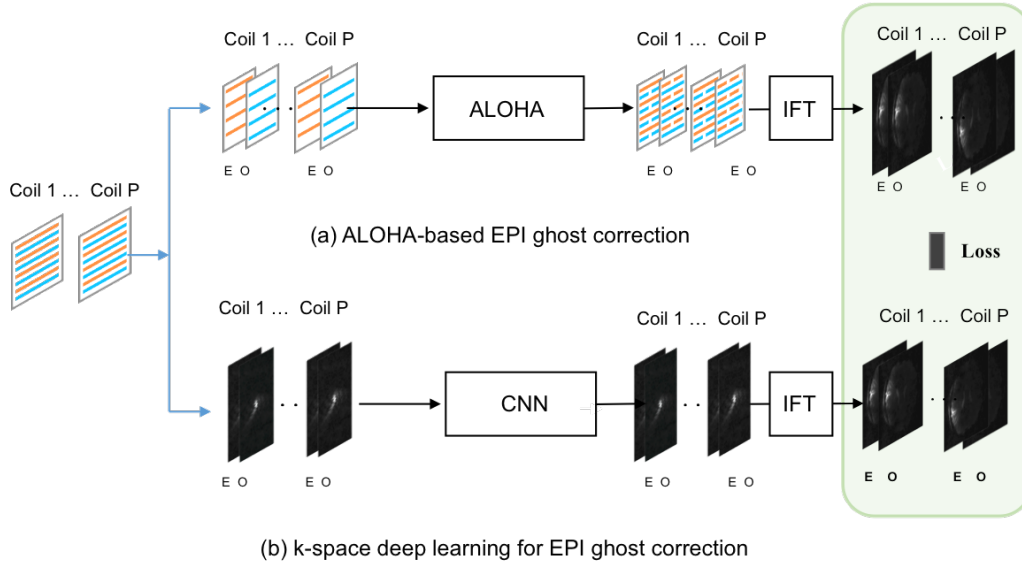


Fig. 1: Reconstruction flow for (a) ALOHA-based ghost artifact removal, and (b)  $k$ -space deep learning for ghost artifact removal. Here, (E) and (O) refers to the frame composed of the even and odd  $k$ -space lines, respectively. After the interpolated even and odd virtual images are generated, the sum-of-squares image is obtained as the final ghost corrected image. Here, IFT stands for the inverse Fourier transform.

redundancy between the coils from the parallel imaging can also be exploited by stacking the multi-coil  $k$ -space data into multi-channel inputs. Our extensive experimentation with 7T in vivo data showed that the proposed  $k$ -space deep learning approaches significantly outperformed existing approaches and even provided robust and accurate ghost corrections for those frames that could not be corrected by ALOHA.

## II. THEORY

### A. ALOHA-based Ghost Correction

To make this paper self-contained, we briefly review the ALOHA-based ghost correction [14]. Specifically, in the presence of off-resonances  $\Delta f(x, y)$ ,  $k$ -space measurement from an EPI sequence can be expressed as [3], [11]:

$$\hat{g}(k_x, k_y) = \int \int \alpha(x, y) e^{\iota 2\pi [\Delta f(x, y) ((TE + (n - N/2)ESP) + (-1)^n (\frac{k_x}{\gamma G_x}))]} \times e^{\iota 2\pi (k_x x + k_y y)} dx dy, \quad (1)$$

where  $\iota = \sqrt{-1}$  and  $k_x$  and  $k_y$  directions represent the read-out and phase-encoding, respectively;  $n$  denotes the phase encoding index in the EPI echo train of total length  $N$ , and  $\alpha(x, y)$  is the transverse magnetization. Here,  $TE$  is the echo time, and  $ESP$  denotes the echo spacing, which is the time between echoes.

The key idea of ALOHA-based ghost correction [14] is to split the original equation in (II-A) into the following two sets of *virtual*  $k$ -space data:

$$\hat{g}_+(k_x, k_y)$$

$$= \int \int \alpha(x, y) e^{\iota 2\pi [\Delta f(x, y) ((TE + (n - N/2)ESP) + (\frac{k_x}{\gamma G_x}))]} \times e^{\iota 2\pi (k_x x + k_y y)} dx dy$$

$$= \int \int A(x, y) e^{\iota 2\pi \Delta f(x, y) \frac{k_x}{\gamma G_x}} \cdot e^{\iota 2\pi (k_x x + k_y y)} dx dy$$

and

$$\hat{g}_-(k_x, k_y)$$

$$= \int \int \alpha(x, y) e^{\iota 2\pi [\Delta f(x, y) ((TE + (n - N/2)ESP) - (\frac{k_x}{\gamma G_x}))]} \times e^{\iota 2\pi (k_x x + k_y y)} dx dy$$

$$= \int \int A(x, y) e^{-\iota 2\pi \Delta f(x, y) \frac{k_x}{\gamma G_x}} \cdot e^{\iota 2\pi (k_x x + k_y y)} dx dy$$

where

$$A(x, y) = \alpha(x, y) e^{\iota 2\pi \Delta f(x, y) (TE + (n - N/2)ESP)}.$$

Then, the even and odd echo signals from the actual EPI measurement can be identified as  $1/2$ -subsampled  $k$ -space data from  $\hat{g}_+(k_x, k_y)$  and  $\hat{g}_-(k_x, k_y)$ , respectively.

The image content for the even and odd virtual data are  $A(x, y) e^{+\iota 2\pi \Delta f(x, y) \frac{k_x}{\gamma G_x}}$  and  $A(x, y) e^{-\iota 2\pi \Delta f(x, y) \frac{k_x}{\gamma G_x}}$ , respectively, which are different from each other. While the difference is the main source of the Nyquist ghost artifacts, they differs only in their phase, so there exists significant redundancy between them. Thus, ALOHA-based EPI correction [14] exploits these redundancy to interpolate the missing virtual  $k$ -space data. More specifically, when two sets of virtual  $k$ -space data are subtracted, we have the following:

$$\hat{g}_\Delta(k_x, k_y) = \hat{g}_{n,+}(k_x, k_y) - \hat{g}_{n,-}(k_x, k_y)$$

$$= \int \int A(x, y) \left( e^{\iota 2\pi \Delta f(x, y) \frac{k_x}{\gamma G_x}} - e^{-\iota 2\pi \Delta f(x, y) \frac{k_x}{\gamma G_x}} \right) \times e^{\iota 2\pi (k_x x + k_y y)} dx dy$$

$$= \int \int A(x, y) 2\iota \sin \left( 2\pi \Delta f(x, y) \frac{k_x}{\gamma G_x} \right) e^{\iota 2\pi (k_x x + k_y y)} dx dy$$

One of the most important observations in [14] is that if the off-resonance  $\Delta f(x, y)$  is sufficiently small, then

$$\sin\left(2\pi\Delta f(x, y)\frac{k_x}{\gamma G_x}\right) \simeq 2\pi\Delta f(x, y)\frac{k_x}{\gamma G_x}. \quad (2)$$

Hence, we have

$$\begin{aligned} \widehat{g}_\Delta(k_x, k_y) &\simeq \iota 2\pi k_x \int \int \frac{2}{\gamma G_x} A(x, y) \Delta f(x, y) \\ &\quad \times e^{\iota 2\pi(k_x x + k_y y)} dx dy \\ &= \frac{2}{\gamma G_x} \mathcal{F} \left[ \frac{\partial A(x, y) \Delta f(x, y)}{\partial x} \right] \end{aligned} \quad (3)$$

where  $\mathcal{F}$  denotes the 2D Fourier transform. Since  $A(x, y)\Delta f(x, y)$  is relatively smooth in most of the images (which is the same assumption for total variation (TV) based modeling), it is easy to see that  $\partial A(x, y)\Delta f(x, y)/\partial x$  is sparse. Even in case where the approximation (2) does not hold, we can expect the even and odd images have high correlation, so the difference should be sparse. In order to appreciate its implication, let  $\mathbf{k}_m = (k_x^{(m)}, k_y^{(m)})$ ,  $m = 1, \dots, M$  be a collection of finite number of sampling points of the  $k$ -space confirming to the Nyquist sampling rate, and the discretized  $k$ -space data be defined by

$$\widehat{\mathbf{g}}_\Delta = \widehat{\mathbf{g}}_+ - \widehat{\mathbf{g}}_-$$

where

$$\begin{aligned} \widehat{\mathbf{g}}_+ &= [\widehat{g}_+(\mathbf{k}_1) \ \cdots \ \widehat{g}_+(\mathbf{k}_M)]^T, \\ \widehat{\mathbf{g}}_- &= [\widehat{g}_-(\mathbf{k}_1) \ \cdots \ \widehat{g}_-(\mathbf{k}_M)]^T, \end{aligned}$$

where the superscript  $T$  denotes the transpose. Due to the sparsity, if we construct a Hankel matrix  $\mathbb{H}_d(\widehat{\mathbf{g}}_\Delta) \in \mathbb{C}^{M \times d}$  from the discretized  $k$ -space data  $\widehat{\mathbf{g}}_\Delta$ , then it is low-ranked [18]. Here,  $d$  denotes the matrix pencil size (for more details on the construction of Hankel matrices and their relation to the convolution, see Appendix A in Supplementary Material or the original reference [20]).

This implies that there exists a vector  $\mathbf{h} \in \mathbb{C}^d$  such that

$$\begin{aligned} \mathbb{H}_d(\widehat{\mathbf{g}}_\Delta)\mathbf{h} &= (\mathbb{H}_d(\widehat{\mathbf{g}}_+) - \mathbb{H}_d(\widehat{\mathbf{g}}_-))\mathbf{h} \\ &= [\mathbb{H}_d(\widehat{\mathbf{g}}_+) \ \mathbb{H}_d(\widehat{\mathbf{g}}_-)] \begin{bmatrix} \mathbf{h} \\ -\mathbf{h} \end{bmatrix} = \mathbf{0} \end{aligned} \quad (4)$$

implying that the concatenated Hankel matrix  $[\mathbb{H}_d(\widehat{\mathbf{g}}_+) \ \mathbb{H}_d(\widehat{\mathbf{g}}_-)] \in \mathbb{C}^{M \times 2d}$  is low-ranked. Similarly, the concatenated Hankel matrix from  $P$  parallel coils is defined as

$$\mathbb{H}_{d|2P}(\widehat{\mathbf{G}}) :=$$

$$\left[ \mathbb{H}_d(\widehat{\mathbf{g}}_+^{(1)}) \ \mathbb{H}_d(\widehat{\mathbf{g}}_-^{(1)}) \ \cdots \ \mathbb{H}_d(\widehat{\mathbf{g}}_+^{(P)}) \ \mathbb{H}_d(\widehat{\mathbf{g}}_-^{(P)}) \right] \quad (5)$$

with  $\mathbb{H}_{d|2P}(\widehat{\mathbf{G}}) \in \mathbb{C}^{M \times 2dP}$  and

$$\widehat{\mathbf{G}} := \begin{bmatrix} \widehat{\mathbf{g}}_+^{(1)} & \widehat{\mathbf{g}}_-^{(1)} & \cdots & \widehat{\mathbf{g}}_+^{(P)} & \widehat{\mathbf{g}}_-^{(P)} \end{bmatrix} \in \mathbb{C}^{M \times 2P}$$

where the superscript denotes the coil index. Then,  $\mathbb{H}_{d|2P}(\widehat{\mathbf{G}})$  is also low-ranked thanks to the inter-coil annihilating filter relationship [17].

Therefore, if some of  $k$ -space data are missing, the missing elements are recovered using low rank Hankel matrix completion approaches [14], [17]–[19], [21]–[25]:

$$(MC) \quad \min_{\widehat{\mathbf{Z}} \in \mathbb{C}^{M \times 2P}} \text{RANK } \mathbb{H}_{d|2P}(\widehat{\mathbf{Z}}) \quad (6)$$

$$\begin{aligned} \text{subject to} \quad &\mathcal{P}_{\Lambda_e}[\widehat{\mathbf{g}}_+^{(i)}] = \mathcal{P}_{\Lambda_e}[\widehat{\mathbf{z}}_{2i-1}], \\ &\mathcal{P}_{\Lambda_o}[\widehat{\mathbf{g}}_-^{(i)}] = \mathcal{P}_{\Lambda_o}[\widehat{\mathbf{z}}_{2i}], \quad i = 1, \dots, P \end{aligned} \quad (7)$$

where  $\widehat{\mathbf{z}}_i$  denotes the  $i$ -th column of  $\widehat{\mathbf{Z}}$ ,  $\Lambda_e$  and  $\Lambda_o$  denote the  $k$ -space indices for the even and odd phase encodings, and  $\mathcal{P}_\Lambda$  denotes the projection to the sampled index  $\Lambda$ . After solving (MC), we can obtain the interpolated even and odd virtual  $k$ -space data for each coil, from which the virtual even and odd images are obtained for each coil by simply taking the inverse Fourier transform. Then, the final artifact corrected EPI data can be obtained as the sum of squares. This procedure of ALOHA-based ghost removal is illustrated in Fig. 1(a).

The low-rank Hankel matrix completion problem (MC) can be solved in various ways, and ALOHA employs the matrix factorization approaches [14], [17], [19]. The main technical problem, however, is the relatively expensive computation costs for the matrix factorization. In the following section, we show that a deep learning approach can address this problem by handling the matrix decomposition completely data-driven.

## B. From ALOHA to Deep Neural Network

In order to understand the link between ALOHA and deep neural network, here we explain the high-dimensional geometry of the low rank Hankel matrix decomposition in Fig. 2, which is the key concept for ALOHA-based EPI ghost correction. More specifically, suppose that  $\widehat{\mathbf{Z}} \in \mathbb{C}^{M \times 2P}$  is lifted to a rank- $Q$  Hankel matrix  $\mathbb{H}_{d|2P}(\widehat{\mathbf{Z}}) \in \mathbb{C}^{M \times 2dP}$ . Then, we can find the two set of basis matrices  $\Psi, \widetilde{\Psi} \in \mathbb{R}^{2dP \times Q}$  and  $\Phi, \widetilde{\Phi} \in \mathbb{C}^{S \times M}$  such that

$$\Psi\widetilde{\Psi}^\top = \mathbf{P}_R, \quad \Phi\widetilde{\Phi}^\top = \mathbf{I}_M, \quad (8)$$

where  $\top$  denotes the Hermitian transpose,  $\mathbf{P}_R$  denotes the projection matrix to the row subspace of  $\mathbb{H}_{d|2P}(\widehat{\mathbf{Z}})$  and  $\mathbf{I}_M$  refers to the  $M \times M$  identity matrix. Using these matrices, it is easy to see that the Hankel matrix  $\mathbb{H}_{d|2P}(\widehat{\mathbf{Z}})$  has the following rank- $Q$  decomposition:

$$\begin{aligned} \mathbb{H}_{d|2P}(\widehat{\mathbf{Z}}) &= \widetilde{\Phi}\Phi^\top \mathbb{H}_{d|2P}(\widehat{\mathbf{Z}}) \Psi\widetilde{\Psi}^\top = \widetilde{\Phi}\mathbf{C}\widetilde{\Psi}^\top \quad (9) \\ &= \sum_{k=1}^S \sum_{l=1}^Q [\mathbf{C}]_{kl} \widetilde{\mathbf{B}}^{kl} \end{aligned} \quad (10)$$

where the basis matrix  $\widetilde{\mathbf{B}}^{kl}$  is defined as

$$\widetilde{\mathbf{B}}^{kl} = \widetilde{\phi}_k \widetilde{\psi}_l^\top, \quad k = 1, \dots, S, \quad l = 1, \dots, Q \quad (11)$$

with  $\widetilde{\phi}_k$  and  $\widetilde{\psi}_l$  denoting the  $k$ -th and  $l$ -th columns of  $\widetilde{\Phi}$  and  $\widetilde{\Psi}$ , respectively. Here, the expansion coefficient  $\mathbf{C} \in \mathbb{C}^{S \times Q}$ , which is often called the convolution framelet coefficients [20], is given by

$$\mathbf{C} := \Phi^\top \mathbb{H}_{d|P}(\widehat{\mathbf{Z}}) \Psi \in \mathbb{C}^{S \times Q} \quad (12)$$

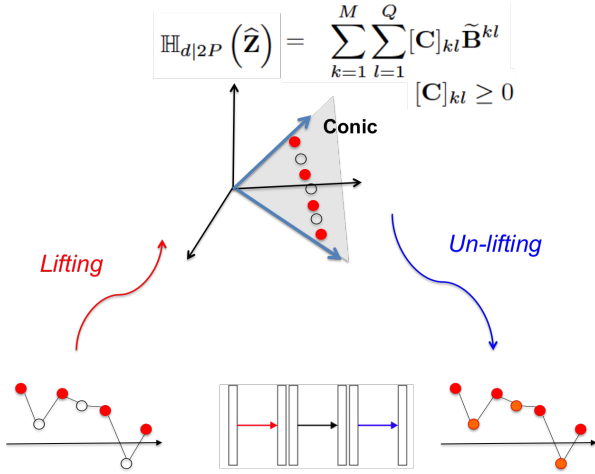


Fig. 2: Geometry of single layer encoder-decoder network for  $k$ -space deep learning. The empty circle corresponds to the missing  $k$ -space data. By lifting to high dimensional space, the missing  $k$ -space data can be easily interpolated.

with  $[\mathbf{C}]_{kl}$  denoting the  $(k, l)$ -element of  $\mathbf{C}$ . Then, the main idea of ALOHA is to find the bases matrices  $\tilde{\mathbf{B}}^{kl}$  such that  $\hat{\mathbf{Z}}$  becomes a feasible solution to  $(MC)$ . In other word, the bases matrices  $\tilde{\mathbf{B}}^{kl}$  are obtained so that  $\mathbb{H}_{d|2P}(\hat{\mathbf{Z}})$  for a feasible solution  $\hat{\mathbf{Z}}$  lives in the span of these bases.

It was shown that ALOHA can be extended to a neural network when the bases matrix  $\tilde{\mathbf{B}}^{kl}$  are obtained from off-line training data [26]. In this case, unlike the original ALOHA, whose basis is obtained from the measurement data, the neural network should learn the basis from the separate training data, so we need some constraints that prevent the learned bases from being arbitrary. In particular, we are interested in the following positivity constraint for the expansion coefficients, i.e.

$$[\mathbf{C}]_{kl} \geq 0, \quad \forall k, l \quad (13)$$

Due to the non-negativity constraint, the training data should be in the conical hull of the base, as shown in Fig. 2, so the learned bases are not very different from the training data. Interestingly, such learned bases result in a part-by-part representation, which is the key ingredient for non-negative matrix factorization (NMF) [27]–[29].

One of the most important findings in the mathematical theory of *deep convolutional framelets* [20] is that when this high dimensional Hankel matrix decomposition is un-lifted to the original signal space, it becomes a neural network with the encoder-decoder architecture. More specifically, by applying the generalized inverse of the Hankel matrix, Eq. (9) can be represented in the original space as follows [20]:

$$\hat{\mathbf{Z}} = (\tilde{\Phi} \mathbf{C}) \circledast \mathcal{G}(\tilde{\Psi}) \quad (14)$$

where  $\circledast$  is the convolution, and  $\mathcal{G}(\tilde{\Psi})$  denotes multi-channel filters that are obtained by rearranging components of  $\tilde{\Psi}$ .

Similarly, (12) can be represented by another convolution [20]:

$$\mathbf{C} = \Phi^\top (\hat{\mathbf{Z}} \circledast \mathcal{H}(\Psi)), \quad (15)$$

where  $\mathcal{H}(\Psi)$  is the multichannel filter obtained by rearranging  $\Psi$ . Furthermore, (13) can be implemented using rectified linear unit (ReLU). Moreover,  $\Phi^\top$  and  $\tilde{\Phi}$  in (15) and (14) are identified as a generalized pooling and unpooling operation [20]. Accordingly, Eqs. (15) and (14) with (13) is indeed one layer CNN with the encoder-decoder architecture as shown in Fig. 2. The idea can be further extended to the multi-layer deep convolutional framelet expansion, when the encoder and decoder convolution filters  $\mathcal{H}(\Psi)$ ,  $\mathcal{G}(\tilde{\Psi})$  can be represented by cascaded convolutions of small length filters. For more details, see [20], [26].

### C. Image Domain Loss

In the  $k$ -space deep learning for accelerated MRI [26], the network is implemented in  $k$ -space domain, while the image domain loss is minimized. In spite of this hybrid architecture, the gradient can be easily calculated, since the adjoint of the Fourier transform is the inverse Fourier transform that can be easily implemented using the fast Fourier transform (FFT) [26]. Therefore, by following the same idea of the  $k$ -space deep learning [26], in the proposed algorithm, ghost corrected images are used as for the label data for network training with the  $l_2$  loss, while the network is implemented in the  $k$ -space.

However, care should be taken in the implementation since the input  $k$ -space data are *virtual* even and odd  $k$ -space data. Thus, we should provide reconstruction images from the interpolated *virtual*  $k$ -space data as labels. Since ALOHA-based ghost correction can interpolate the virtual even and odd  $k$ -data, we therefore use the reconstruction results from these interpolated  $k$ -space data as our label. Specifically, as shown in Fig. 1(a)(b), the even and odd virtual images are generated using ALOHA for each coil from ghost corrected even and odd  $k$ -space lines. Then, these even and odd complex images for each coils are used as label data.

## III. METHOD

The raw data were acquired by 7T whole body scanner for 8 healthy subjects (Philips Achieva system) using 32 channel phased-array RF coils. The acquisition parameters are as followed: TR/TE = 3000/24ms, Flip angle = 90°, Field of View(FOV) = 192 × 192mm<sup>2</sup>, voxel size = 2.7 × 2.7mm<sup>2</sup>, slice thickness = 2.7mm. Gradient-recalled echo EPI (GRE-EPI) sequence was used, and the acquired data is composed of 40 slices and 60 temporal frames. The pre-scan data for conventional ghost correction method is also acquired before the whole data acquisition. This pre-scan data is acquired for all PE lines, slices and coils without phase encoding blips. The phase difference is calculated by subtracting a phase of one PE line from a phase of adjacent PE line. Then the phase mismatch of image is compensated by the calculated phase difference map. Also, the reference-free ghost correction algorithm in [12] is implemented. In this algorithm, phase disparity is calculated from  $x - k_y$  domain raw data by assuming the disparity is linear along the readout direction.

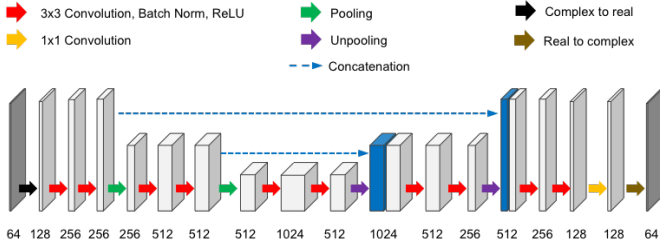


Fig. 3: The proposed network backbone for the 64 channel 7T EPI data ghost correction.

The overall reconstruction flow of the proposed  $k$ -space deep learning-based ghost correction method is illustrated in Fig. 1(b). Specifically, the  $P$  channel multi-coil  $k$  space data is divided into even and odd channels. Then, the even and odd  $k$ -space data are processed using the convolutional neural network, whose output is the interpolated even and odd  $k$ -space data for each coil. Then, the inverse Fourier transform is applied to obtain the ghost corrected virtual even and odd images. Finally, similar to ALOHA, the sum-of-squares images are generated from the even and odd images from multiple channels. In fact, this procedure is exactly the same at the ALOHA-based ghost correction algorithm in Fig. 1(a), except for the  $k$ -space interpolation step. Specifically,  $k$ -space interpolation is done using ALOHA in Fig. 1(a), whereas it is done using CNN in Fig. 1(b). Another minor difference is that ALOHA uses the zero-padded even and odd  $k$ -space data as input, whereas in the proposed method we augmented the missing  $k$ -space lines with the other phase  $k$ -space data to make the network training converge faster.

Fig. 3 illustrates a multi-scale neural network backbone employed in the proposed method. Specifically, the network backbone is based on U-net structure [30] composed of convolution layers with batch normalization and ReLU, pooling layer, and contracting path with concatenation. Here, red arrow refers to the basic unit of this network that consists of several  $3 \times 3$  convolution layers with batch normalization and rectified linear unit (ReLU) after every convolution layer. Also,  $2 \times 2$  average pooling (green arrow) and unpooling layers (purple arrow) are inserted after two basic unit layers. Some of intermediate image on encoding process is concatenated with unpooled image (blue arrow). The yellow arrow which is located at the end of network, indicates  $1 \times 1$  convolution. As the input  $k$ -space and output image data are complex-value, so we first divide the complex-valued  $k$ -space data into real and imaginary channels as suggested in [26] before inputting them to U-Net backbone. This operator is shown in Fig. 3 as black arrow. Accordingly, the number of channels are doubled because this step separates real and imaginary value of  $k$ -space and concatenates them through channel direction. Similarly, at the network output, the real-valued real and imaginary channels are combined to obtain complex-valued  $k$ -space data (brown arrow).

As discussed before, we used the ALOHA-based ghost correction images as label. However, as will be shown later, for high-field MRI, the ALOHA-based correction algorithm often

fail to remove the ghost artifacts in some frames. Therefore, we visually inspected ALOHA-based ghost correction results, chose the ones with ghost corrected  $k$ -space data, and use them as labels. Interestingly, as will be shown later, our trained neural network then successfully corrects the ghost artifacts even from the cases where ALOHA fails.

The network was implemented using MatConvNet toolbox (ver.24) in MATLAB 2015a environment (Mathwork, Natick). We used a GTX 1080-Ti graphic processor and i7-4770 CPU (3.40GHz). The weights of convolutional layers were initialized by Gaussian random distribution with Xavier method to achieve proper scale. This helps us to avoid the signal to be exploded or vanished in the initial phase of learning. The stochastic gradient descent (SGD) method with momentum was used to train the weights of the network and minimized the loss function. In training, the number of epochs was 30 to avoid overfitting, and the size 4 mini batch is used. The learning rate is started from  $10^{-5}$ , and gradually decreased to  $10^{-6}$ . To prevent the weight becoming too large, the regularization parameter is used as  $10^{-4}$ . Also, we used  $l_2$  loss of image domain data for training. Training time was 2.5 hours. The number of subjects are 8, among which 6 subject is used for training, other 1 subject is used as validation, and the other subject is used as test.

To see the benefits of  $k$ -space learning over image learning, the same network architecture in Fig. 3 was used for image-domain learning. In this case, the input data were not the  $k$ -space data but the even and odd virtual images damaged with ghost artifacts, and the training goal is to learn the relationship between these input images and output ghost corrected virtual images. The same training procedure as described above was used for the image-domain learning.

#### IV. RESULTS

The ghost correction results from 7T EPI data are shown in Fig. 4. The proposed method corrected ghost artifacts for the different brain structure and size. The proposed method shows the lowest ghost artifacts in all the cases. However, as shown in the magnified view, there are remaining ghost artifact and streak artifact on the results by ALOHA, and the conventional reference-based and reference-free methods. In addition, there is a ringing artifact in ALOHA results, and the texture is blurred compared to the result of the proposed method.

To evaluate the performance of each method quantitatively, we calculated the ghost-to-signal ratio (GSR) of results. The GSR is defined as the magnitude ratio between ghost region and non-ghost region, and it is indicated by percent value [14]. Fig. 5 shows the ghost correction results of various methods. The first line shows the ghost corrected images and the second line is for the rescaled images at 20% of magnitude. The GSR values corresponding to each result are calculated using regions represented by the white boxes and marked on the image. As shown in this result, the proposed method successfully removed ghost artifacts and shows the lowest GSR value. As for results of ALOHA, there is a remaining ghost artifact on the scaled image (yellow arrow). In addition,

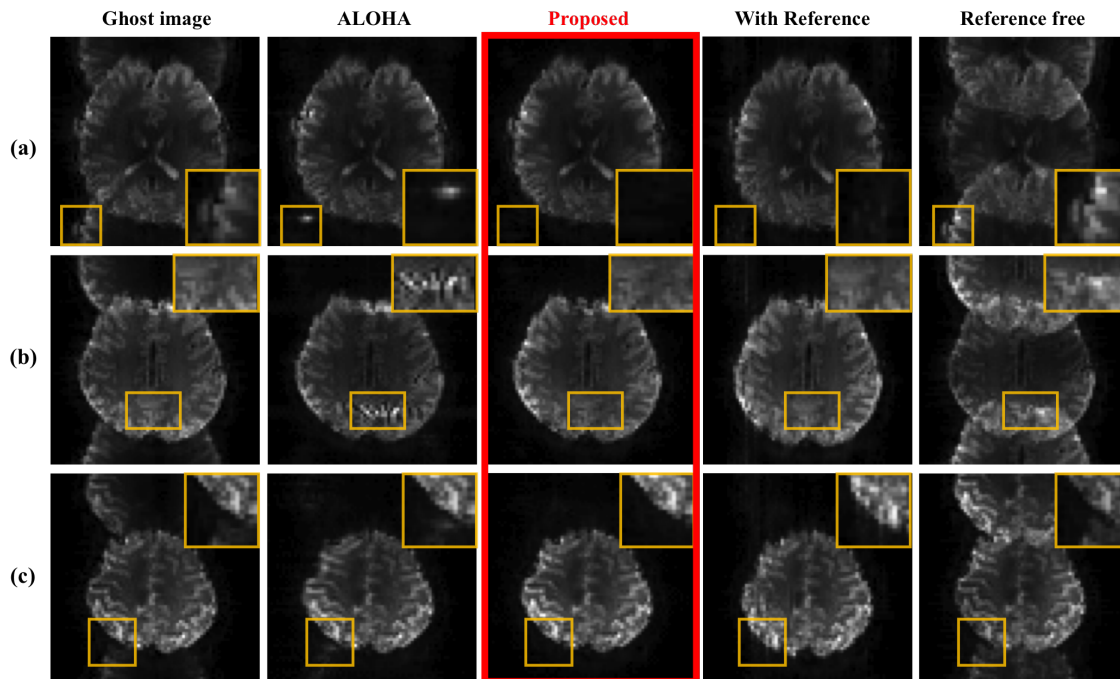


Fig. 4: Ghost correction results by various methods. In the rescaled- and magnified boxes, there are still remaining ghost and streak artifacts in the conventional methods.

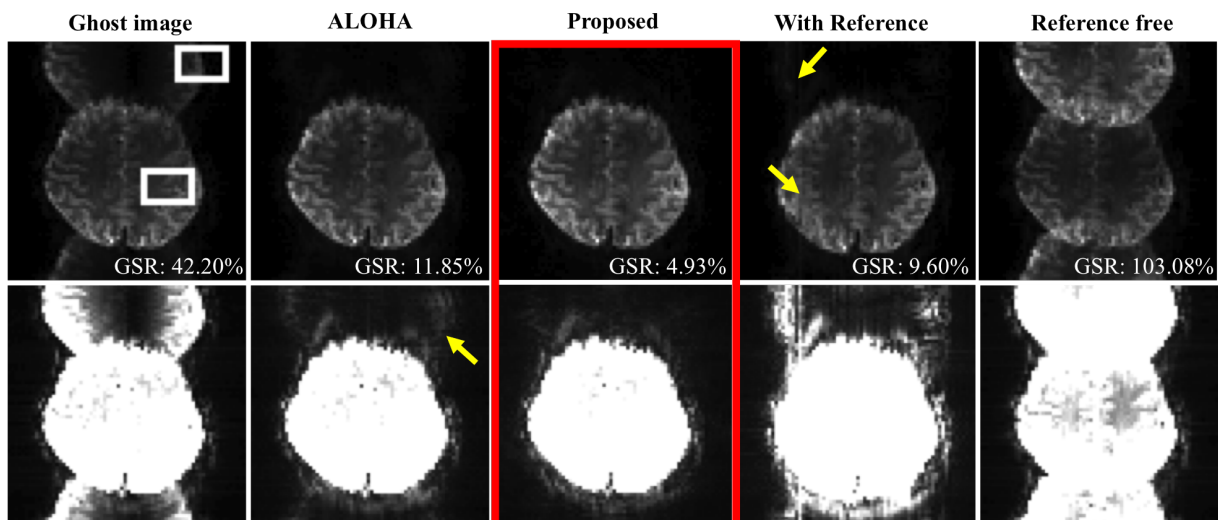


Fig. 5: Quantitative evaluation of various ghost correction method. Ghost artifacts are very well removed by the proposed method, while the remaining artifact is shown in the result of ALOHA and conventional methods (yellow arrow).

the streak artifact and the remaining ghost artifact are observed on the result of the reference-based method. The reference-free correction method shows severe ghost artifacts.

Fig. 6 compares the image-domain deep learning results with the proposed  $k$ -space deep learning method. Similar to the observation in the  $k$ -space learning for accelerated MRI [26], both approaches work. However, if we look at the details in the rescaled- and magnified boxes, there are still remaining ghost artifacts in the image-domain learning (Fig. 6(b)), and the internal image structure is a bit blurry compared to the  $k$ -

space learning due to the removal of the true signal as shown in the difference images in Fig. 6(a).

## V. DISCUSSION

It is known that 7T EPI data is quite sensitive to the local field inhomogeneity, and the phase change is also large and nonlinear [31]. Therefore, the reference-based method which obtains a pre-scan from MR is often not possible to perform the phase correction completely. On the other hand, ALOHA is a low-rank based approach that works well if the matrix pencil

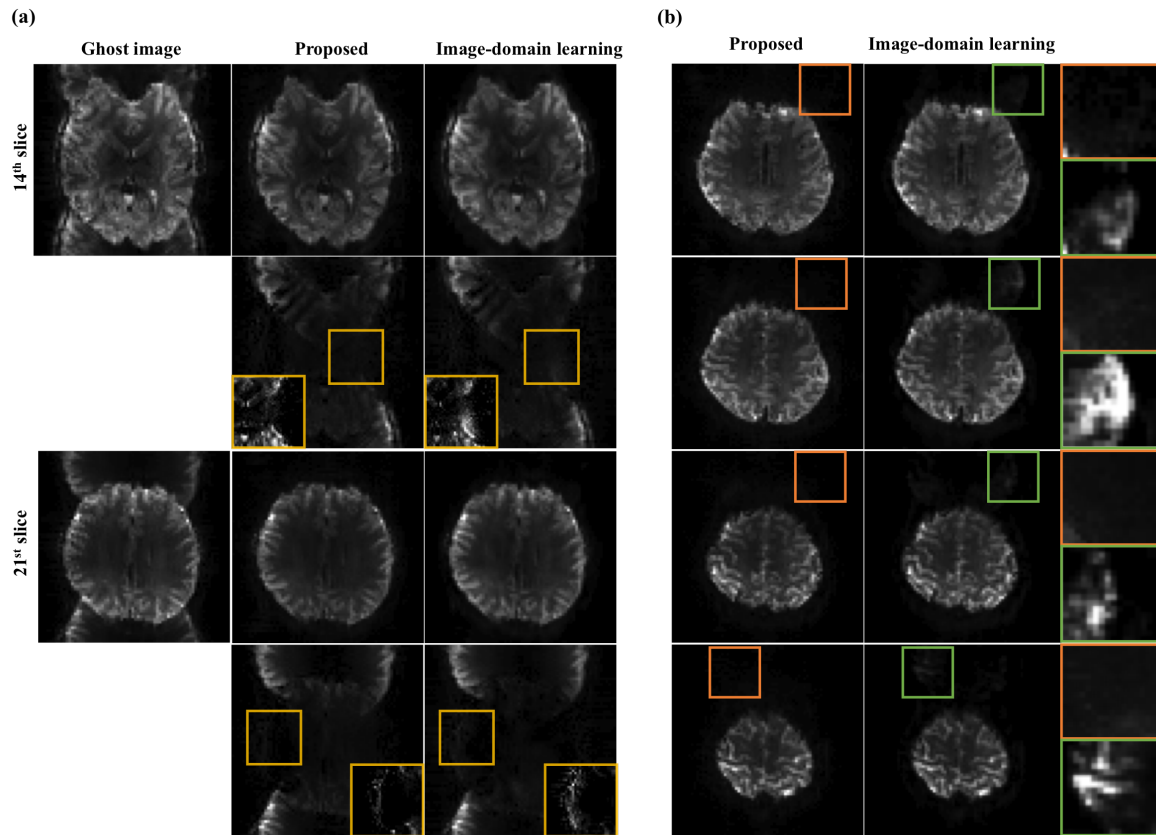


Fig. 6: Comparison with the image-domain learning. In the rescaled- and magnified boxes, there are still remaining ghost artifacts in the image-domain learning, and the internal image structure is a bit blurry compared to the  $k$ -space learning.

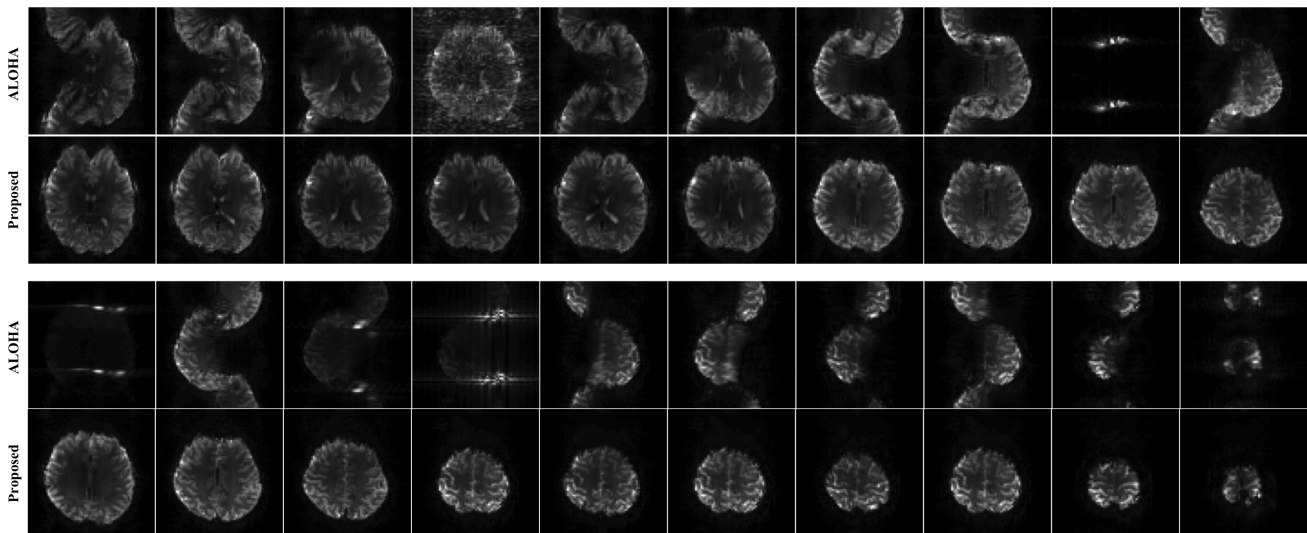


Fig. 7: Robustness of the proposed method. Even for the failure cases by ALOHA, the proposed method successfully corrected the ghost artifacts.

size in the construction of the Hankel matrix should be greater than the intrinsic rank. Unlike the 3T EPI data, we found that a similar matrix pencil size does not work for 7T size due to the larger local field inhomogeneity variations. One could increase the matrix pencil size for the Hankel matrix, but the associated

memory and computational complexity increases are sometime not durable in real applications. Moreover, with bigger matrix pencil size, the algorithm became more sensitive to other hyperparameters. Thus, ghost correction using ALOHA on 7T MR shows many failure cases. Specifically, from 14,400 set

of training data set in our experiment, we could get the only 2040 successful cases for ghost correction using the ALOHA. Thus, only 2040 successful cases are used as label data for our neural network training.

Fig. 7 shows representative failure cases from the test data by the ALOHA-based ghost correction for 7T data. Interestingly, as shown in Fig. 7, even for the failure cases by ALOHA, the proposed method successfully corrected the ghost artifacts. In fact, among 2400 test data set, no failure cases were observed using the proposed  $k$ -space deep learning approach for ghost correction. This shows that the proposed algorithm is very robust even under large local field inhomogeneity changes.

	Reference based	ALOHA	Proposed
Time/slice	138.7ms	48,685ms	17ms

TABLE I: Ghost correction time by various methods.

The computational times for ghost correction by various methods are shown in Table I. The computational time was calculated for each single slice using 64 parallel coil  $k$ -space data as input. The proposed method took only 17ms for each slice, which is several order of magnitude faster than the conventional methods. This confirms the practicability of the proposed method.

## VI. CONCLUSION

In this study, we proposed a new ghost artifact correction method using  $k$ -space deep learning. The proposed  $k$ -space deep learning with an image domain loss was derived based on the recent mathematical discovery that a deep convolutional neural network is closely related to the Hankel matrix decomposition. The ghost correction results using 7T data confirmed that the proposed method significantly outperformed the existing approaches in the image quality and the reconstruction time. Moreover, the proposed method were very robust and successfully removed the ghost artifacts even when ALOHA-based approach failed. Therefore, we believe that this opens a new direction for EPI ghost correction.

## REFERENCES

- [1] C. Z. Ahn CB, "A new phase correction method in nmr imaging based on autocorrelation and histogram analysis," *IEEE Trans. Med. Imag.*, vol. 6, no. 1, pp. 32–36, 1987.
- [2] R. H.-E. Bruder H, Fischer H and S. F, "Image reconstruction for echo planar imaging with nonequidistant k-space sampling," *Magn. Reson. Med.*, vol. 23, no. 2, pp. 311–323, 1992.
- [3] L. T. Hu X, "Artifact reduction in EPI with phase-encoded reference scan," *Magn. Reson. Med.*, vol. 36, no. 1, pp. 166–171, 1996.
- [4] A. E.-M. E. Reeder SB, Faranesh AZ, "A novel object-independent balanced reference scan for echo-planar imaging," *Journal of Magnetic Resonance Imaging*, vol. 9, no. 6, p. 847, 1999.
- [5] Y. F. Xiang Q-S, "Correction for geometric distortion and N/2 ghosting in EPI by phase labeling for additional coordinate encoding (PLACE)," *Magn. Reson. Med.*, vol. 57, no. 4, pp. 731–741, 2007.
- [6] M. E. Kellman P, "Phased array ghost elimination," *NMR in Biomedicine*, vol. 19, no. 3, pp. 352–361, 2006.
- [7] B. MH and Z. DC, "Image-based ghost correction for interleaved EPI," *Magn. Reson. Med.*, vol. 45, no. 1, pp. 96–108, 2001.
- [8] C. N-K and W. AM, "Removal of EPI nyquist ghost artifacts with twodimensional phase correction," *Magn. Reson. Med.*, vol. 51, no. 6, pp. 1247–1253, 2004.
- [9] H. WS, T. H, and kraft RA, "Robust EPI nyquist ghost elimination via spatial and temporal encoding," *Magn. Reson. Med.*, vol. 64, no. 6, pp. 1781–1791, 2010.
- [10] L. B.-S. M. Yang QX, Posse S, "Double-sampled echo-planar imaging at 3 tesla," *Journal of Magnetic Resonance, Series B*, vol. 113, no. 2, pp. 145–150, 1996.
- [11] G. P.-D. W. S. V. Poser BA, Barth M, "Single-shot echo-planar imaging with Nyquist ghost compensation: Interleaved dual echo with acceleration (IDEA) echo-planar imaging (EPI)," *Magn. Reson. Med.*, vol. 69, no. 1, pp. 37–47, 2013.
- [12] W. F. Zhang Y, "Reference-scan-free method for automated correction of nyquist ghost artifacts in echoplanar brain images," *Magn. Reson. Med.*, vol. 51, pp. 621–624, 2004.
- [13] N. R.-M. M. B. R. Skare S, Clayton DB, "A fast and robust minimum entropy based non-interactive nyquist ghost correction algorithm," *Magn. Reson. Med.*, vol. 51, pp. 621–624, 2004.
- [14] J. Lee, K. H. Jin, and J. C. Ye, "Reference-free single-pass EPI Nyquist ghost correction using annihilating filter-based low rank Hankel matrix (ALOHA)," *Magnetic resonance in medicine*, 2016.
- [15] M. Mani, M. Jacob, D. Kelley, and V. Magnotta, "Multi-shot sensitivity-encoded diffusion data recovery using structured low-rank matrix completion (MUSSELS)," *Magnetic resonance in medicine*, vol. 78, no. 2, pp. 494–507, 2017.
- [16] R. A. Lobos, T. H. Kim, W. S. Hoge, and J. P. Haldar, "Navigator-free EPI ghost correction using low-rank matrix modeling: Theoretical insights and practical improvements," in *Proc. Int. Soc. Magn. Reson. Med.*, 2017, p. 0449.
- [17] K. H. Jin, D. Lee, and J. C. Ye, "A general framework for compressed sensing and parallel MRI using annihilating filter based low-rank Hankel matrix," *IEEE Transactions on Computational Imaging*, vol. 2, no. 4, pp. 480–495, 2016.
- [18] J. C. Ye, J. M. Kim, K. H. Jin, and K. Lee, "Compressive sampling using annihilating filter-based low-rank interpolation," *IEEE Transactions on Information Theory*, vol. 63, no. 2, pp. 777–801, 2017.
- [19] D. Lee, K. H. Jin, E. Y. Kim, S.-H. Park, and J. C. Ye, "Acceleration of MR parameter mapping using annihilating filter-based low rank hankel matrix (ALOHA)," *Magnetic resonance in medicine*, vol. 76, no. 6, pp. 1848–1864, 2016.
- [20] J. C. Ye, Y. Han, and E. Cha, "Deep convolutional framelets: A general deep learning framework for inverse problems," *SIAM Journal on Imaging Sciences*, vol. 11, no. 2, pp. 991–1048, 2018.
- [21] E. J. Candès and B. Recht, "Exact matrix completion via convex optimization," *Found. Comput. Math.*, vol. 9, no. 6, pp. 717–772, 2009.
- [22] J.-F. Cai, E. J. Candès, and Z. Shen, "A singular value thresholding algorithm for matrix completion," *SIAM J. Optimiz.*, vol. 20, no. 4, pp. 1956–1982, 2010.
- [23] E. J. Candès and T. Tao, "The power of convex relaxation: Near-optimal matrix completion," *IEEE Trans. Inf. Theory*, vol. 56, no. 5, pp. 2053–2080, 2010.
- [24] D. Gross, "Recovering low-rank matrices from few coefficients in any basis," *Information Theory, IEEE Transactions on*, vol. 57, no. 3, pp. 1548–1566, 2011.
- [25] R. H. Keshavan, A. Montanari, and S. Oh, "Matrix completion from a few entries," *IEEE Trans. Inf. Theory*, vol. 56, no. 6, pp. 2980–2998, 2010.
- [26] Y. Han and J. C. Ye, "k-Space Deep Learning for Accelerated MRI," *arXiv preprint arXiv:1805.03779*, 2018.
- [27] D. D. Lee and H. S. Seung, "Unsupervised learning by convex and conic coding," in *Advances in neural information processing systems*, 1997, pp. 515–521.
- [28] —, "Learning the parts of objects by non-negative matrix factorization," *Nature*, vol. 401, no. 6755, p. 788, 1999.
- [29] —, "Algorithms for non-negative matrix factorization," in *Advances in neural information processing systems*, 2001, pp. 556–562.
- [30] O. Ronneberger, P. Fischer, and T. Brox, "U-net: Convolutional networks for biomedical image segmentation," in *International Conference on Medical image computing and computer-assisted intervention*. Springer, 2015, pp. 234–241.
- [31] W. S. Hoge and J. R. Polimeni, "A dual-polarity GRAPPA kernel for the robust reconstruction of accelerated EPI data," in *Biomedical Imaging (ISBI), 2015 IEEE 12th International Symposium on*. IEEE, 2015, pp. 1244–1247.

## SUPPLEMENTARY MATERIAL

### APPENDIX A

For simplicity, here we consider 1-D signals, but its extension to 2-D is straightforward. In addition, to avoid separate treatment of boundary conditions, we assume periodic boundary. Let  $\mathbf{f} \in \mathbb{C}^N$  be the signal vector. Then, a single-input single-output (SISO) convolution of the input  $\mathbf{f}$  and the length  $d$ -filter  $\bar{\mathbf{h}} \in \mathbb{R}^d$  can be represented in a matrix form:

$$\mathbf{y} = \mathbf{f} \circledast \bar{\mathbf{h}} = \mathbb{H}_d(\mathbf{f})\mathbf{h}, \quad (16)$$

where  $\mathbb{H}_d(\mathbf{f})$  is a wrap-around Hankel matrix defined by

$$\mathbb{H}_d(\mathbf{f}) = \begin{bmatrix} [\mathbf{f}]_1 & [\mathbf{f}]_2 & \cdots & [\mathbf{f}]_d \\ [\mathbf{f}]_2 & [\mathbf{f}]_3 & \cdots & [\mathbf{f}]_{d+1} \\ \vdots & \vdots & \ddots & \vdots \\ [\mathbf{f}]_N & [\mathbf{f}]_1 & \cdots & [\mathbf{f}]_{d-1} \end{bmatrix} \quad (17)$$

where  $d$  denotes the matrix pencil parameter. On the other hand, multi-input multi-output (MIMO) convolution for the  $P$ -channel input  $\mathbf{Z} = [\mathbf{z}_1, \dots, \mathbf{z}_P]$  to generate  $Q$ -channel output  $\mathbf{Y} = [\mathbf{y}_1, \dots, \mathbf{y}_Q]$  can be represented by

$$\mathbf{y}_i = \sum_{j=1}^P \mathbf{z}_j \circledast \bar{\boldsymbol{\psi}}_i^j, \quad i = 1, \dots, Q \quad (18)$$

where  $\bar{\boldsymbol{\psi}}_i^j \in \mathbb{R}^d$  denotes the length  $d$ -filter that convolves the  $j$ -th channel input to compute its contribution to the  $i$ -th output channel. By defining the MIMO filter kernel  $\boldsymbol{\Psi}$  as follows:

$$\boldsymbol{\Psi} = \begin{bmatrix} \boldsymbol{\Psi}_1 \\ \vdots \\ \boldsymbol{\Psi}_P \end{bmatrix} \quad \text{where} \quad \boldsymbol{\Psi}_j = \begin{bmatrix} \boldsymbol{\psi}_1^j & \cdots & \boldsymbol{\psi}_Q^j \end{bmatrix} \in \mathbb{R}^{d \times Q} \quad (19)$$

the corresponding matrix representation of the MIMO convolution is then given by

$$\mathbf{Y} = \mathbf{Z} \circledast \bar{\boldsymbol{\Psi}} \quad (20)$$

$$= \sum_{j=1}^P \mathbb{H}_d(\mathbf{z}_j) \boldsymbol{\Psi}_j \quad (21)$$

$$= \mathbb{H}_{d|P}(\mathbf{Z}) \boldsymbol{\Psi} \quad (22)$$

where  $\bar{\boldsymbol{\Psi}}$  is a flipped block structured matrix:

$$\bar{\boldsymbol{\Psi}} = \begin{bmatrix} \bar{\boldsymbol{\Psi}}_1 \\ \vdots \\ \bar{\boldsymbol{\Psi}}_P \end{bmatrix} \quad \text{where} \quad \boldsymbol{\Psi}_j = \begin{bmatrix} \bar{\boldsymbol{\psi}}_1^j & \cdots & \bar{\boldsymbol{\psi}}_Q^j \end{bmatrix} \in \mathbb{R}^{d \times Q} \quad (23)$$

and  $\mathbb{H}_{d|P}(\mathbf{Z})$  is an *extended Hankel matrix* by stacking  $P$  Hankel matrices side by side:

$$\mathbb{H}_{d|P}(\mathbf{Z}) := \begin{bmatrix} \mathbb{H}_d(\mathbf{z}_1) & \mathbb{H}_d(\mathbf{z}_2) & \cdots & \mathbb{H}_d(\mathbf{z}_P) \end{bmatrix}. \quad (24)$$